Monolayer MoS$_2$ anchored on reduced graphene oxide nanosheets for efficient hydrodesulfurization

Lan Yang [a], Xu-zhen Wang [a,b,*], Yang Liu [b], Zheng-fa Yu [b], Jing-jing Liang [b], Bing-bing Chen [a,c], Chuan Shi [a,c], Song Tian [a], Xiang Li [a], Jie-shan Qiu [a,b]

[a] State Key Laboratory of Fine Chemicals and School of Chemistry, Faculty of Chemical, Environmental & Biological Science and Technology, Dalian University of Technology, Dalian, China
[b] Carbon Research Laboratory, Liaoning Key Laboratory for Energy Materials & Chemical Engineering, Faculty of Chemical, Environmental & Biological Science and Technology, Dalian University of Technology, Dalian, China
[c] Key Laboratory of Industrial Ecology and Environmental Engineering (MOE), Dalian University of Technology, Dalian, China

ARTICLE INFO

ABSTRACT

Highly active monolayer MoS$_2$/reduced graphene oxide (ML-MoS$_2$/RGO) catalysts have been fabricated with the assistance of cetyltrimethylammonium bromide via a solution route. The as-prepared catalysts are systematically investigated by X-ray diffraction, Raman spectra, field emission scanning electron microscopy and high-resolution transmission electron microscopy. Layer-depended catalytic performance of MoS$_2$ active component has been demonstrated in the model hydrodesulfurization reaction of carbonyl sulfide. The ML-MoS$_2$/RGO composites show superior catalytic activity compared with few-layer MoS$_2$/RGO (FL-MoS$_2$/RGO) catalyst or bulk MoS$_2$ with multilayer structure, which can be ascribed to more exposure of MoS$_2$ active sites on monolayer MoS$_2$ combined with high dispersion of monolayer MoS$_2$ nanoparticles on RGO sheets. This work offers a facile strategy for the synthesis of monolayer MoS$_2$ supported on RGO for efficient catalysis applications.

© 2016 Elsevier B.V. All rights reserved.

1. Introduction

Carbonyl sulfide (COS), one of the main organic sulfur compounds widely existing in natural gas, water gas, petroleum gas, and industrial tail gas, is normally regarded as a significant poison for industrial catalysis [1]. Hydrodesulfurization (HDS) is an efficient way for the removal of COS because hydrogen can act as both reducing agent and hydrogenation agent [2]. Currently, commercial HDS processes generally use molybdenum disulfide (MoS$_2$) catalysts, most often supported on Al$_2$O$_3$ or SBA-15 and promoted with Co or Ni [3–6]. In order to clarify the effects of supports or promoters, unsupported MoS$_2$ has also been investigated as a model catalyst in studies of HDS reactions [7–10]. Traditional MoS$_2$ particles loaded catalysts have been extensively studied for many years [11,12], and the desulfurization performance of MoS$_2$ particles at low temperature is still a challenge due to its low dispersion and less exposed active sites.

MoS$_2$ is a kind of layered inorganic compound which can be exfoliated to monolayer graphene-like structure. Inspired by the graphene, the activity of HDS may be improved by some ways such as reducing the size of MoS$_2$ particles [13–15], exfoliating the layers of MoS$_2$ [16] and enhancing the dispersion of MoS$_2$ in composites [17,18]. It is necessary to understand the relationship between active sites and the structure of MoS$_2$ catalyst for the improvement of the catalytic performance, and a number of efforts have been made focusing on the structure-activity relationship for MoS$_2$ catalysts [19,20]. The activity of MoS$_2$ is closely related to the edge planes of MoS$_2$. Eijsbouts et al. have shown a clear correlation between HDS conversion and the number of Mo atoms at the corners and edges of MoS$_2$ crystallites, reported as the MoS$_2$ dispersion. High-activity commercial catalysts are found to have very high MoS$_2$ dispersions [21]. Thian et al. examined the HDS of dibenzothiophene (DBT) over a series of MoS$_2$ catalysts with different morphology and drew a conclusion that exfoliated MoS$_2$ hold the most excellent performance [16]. The large size and the bulk phase of materials would restrict the complete use of active sites. MoS$_2$ vertically grown on carbon cloth results in abundant active-edges exposure and effective electron delivery, as a result, it shows

excellent activity in hydrogen evolution reaction [22]. High catalytic activity in HDS reaction of thiophene over three-dimensional (3D) material consisting of assembled single-layer MoS_2 nanotubes with more active sites has also been demonstrated [23].

Recently, carbon materials have often been used for elaboration of model hydrotreating catalyst [24,25]. CoMo carbon-supported catalysts were found to be more active than alumina-supported for both DBT and 4,6-dimethyldibenzothiophene (4,6-DBT) hydrodesulfurization [26]. Moreover, it is well admitted that carbon-supported CoMoS is more weakly bound to the support than oxide supports, this weak interaction being responsible for a higher catalytic activity [27]. However, the traditional activated carbon was easily blocked by loading metal due to its smaller aperture, and it is not conducive to the spread of the reactants or products and bad for the removal of sulfur. Graphene, as a new star of carbon materials, has attracted wide attention due to its unique physical, chemical and mechanical properties [28,29]. It shows potential applications in many fields such as energy storage [30], photocatalysis [31], chemical sensors [32] and so on. Graphene is also regarded as a promising matrix for supported catalyst [33] because of its high surface area (theoretical value of 2630 $m^2\,g^{-1}$) [30], stable graphitic basal plane structure, good conductivity, and a potential for large scale production at a moderate cost [28,29]. Mesoporous graphene [34], crumpled graphene balls [35], as well as CNT/graphene composites [36] as loading substrates have been designed to construct 3D structures with more active edges exposed. In recent years, there is an increasing interest in the synthesis of heterostructures of monolayer MoS_2 and graphene based on their similar two-dimensional (2D) morphology [37,38]. Previous reports have been focused on the preparation of MoS_2/graphene hybrids and investigation of their synergistic interactions which can greatly improve their properties for various applications, such as photocatalysis, photodetection, photoconductivity and catalytic activity, however, the application of the monolayer MoS_2/graphene hybrid in the hydrodesulfurization of COS has not been demonstrated [39–43]. Compared with traditional alumina-supported catalyst, graphene was regarded as both adsorption and catalyst [44]. Graphene supported monolayer MoS_2 catalyst may hold effective activity because of the combination of physical adsorption, chemical adsorption and catalytic reaction.

Herein, monolayer MoS_2 was uniformly loaded on reduced graphene oxide nanosheets (ML-MoS_2/RGO) through a modified CTAB-assisted solution route. The obtained catalyst displays an efficient HDS activity for COS conversion especially at low temperatures (below 220 °C). The layer-depended catalytic performance of MoS_2 active component has been demonstrated, indicating that ML-MoS_2/RGO shows superior activity compared with few layer-MoS_2/RGO and bulk MoS_2 in the low temperature range.

2. Experimental

2.1. Synthesis of catalysts

Graphene oxide (GO) was prepared by a modified Hummers method [45] from nature graphite powder (Qingdao Black Dragon Graphite Co. Ltd.). ML-MoS_2/RGO composites were synthesized by a modified CTAB-assisted solution method [46]. In a typical procedure, GO (5.4 mg/mL, 32 mL) was added to 100 mL of distilled water containing CTAB (3.64 g, 10 mM) and the mixture was stirred at 40 °C in a water bath for 24 h to allow CTA^+ ions well adsorbed on the GO surface. After that, excessive ammonium tetrathiomolybdate (ATTM, 0.70 g, home-made from ammonium heptamolybdate and ammonium sulfide by a solution reaction [47]) were dispersed in distilled water (30 mL) with ultrasonication for 5 min and added into the above solution. Then, hydrazine hydrate (80%, 10 mL) as a

reducing agent was added with continuous stirring. The reaction mixture was transferred into a round bottom flask (250 mL volume) equipped with a condenser tube, and refluxed at 95 °C for 8 h. The precipitates were collected by filtration, washed with distilled water and ethanol for several times, and dried at 60 °C in a vacuum oven. Finally, the composites were annealed in a conventional tube furnace at 800 °C for 2 h in nitrogen to form the ML-MoS_2/RGO composites.

For comparison, few layer MoS_2 supported on reduced graphene oxide (FL-MoS_2/RGO) without the presence of CTAB and bulk MoS_2 (B-MoS_2) without the presence of CTAB and GO were also prepared by the same procedure as mentioned above.

2.2. Characterization

The powder X-ray diffraction (XRD) patterns were recorded on a Rigaku D/max 2400 Diffractometer using Cu Kα radiation (λ = 0.15418 nm). Raman measurements were performed with a micro-Raman spectrometer (Thermo Fisher Scientific DXR) with the excited wavelength of 532 nm. The morphology and size of the catalysts were observed under scanning electron microscopy (SEM, FEI Quanta 400 FESEM), and high-resolution transmission electron microscopy (HRTEM, FEI TecnaiF30). Thermal gravimetric analyses (TGA, DTG-60AH) were measured in air with temperature range from 30 to 700 °C at a heating rate of 10 °C min^{-1}. Fourier transform infrared (FT-IR) spectra (4000–500 cm^{-1}) in KBr were collected on an EQUINOX55 spectrometer. The acidity of catalyst was measured by temperature programmed desorption of ammonia (NH_3-TPD) in a TP-5000 quartz micro reactor (CHEMBET-3000). About 100 mg of catalyst sample was pretreated at 500 °C for 2 h in an Ar flow of 50 mL min^{-1}, cooled down to 120 °C. Then it was saturated with dry ammonia through pulse-injection. The sample was flushed further with the Ar flow at 120 °C for 1 h to remove any physically adsorbed ammonia. After that, the sample was heated from 120 °C to 650 °C at a heating rate of 10 °C min^{-1} and the amount of NH_3 desorbed was measured with the TCD. The active sites were measured by CO pulse adsorption (Autochem II 2920, Micromeritics, USA). Each sample (30 mg) was pretreated at 500 °C for 60 min in He flow. Then it was subsequently cooled down to room temperature, 5% CO/He was injected in pulses until saturated adsorption was reached.

2.3. Test of HDS activity and kinetic studies

The catalytic reactions were carried out in a continuous up-flow fixed-bed quartz reactor (6 mm × 430 mm) heated in a furnace at atmospheric pressure (shown in Fig. S4). The as-prepared catalyst (50 mg) was put in the center of the quartz reactor. The catalytic activity for COS hydrogenation was evaluated in reactant gases (500 ppm COS, 10 vol% H_2, balanced with N_2, GHSV = 32000 h^{-1}) under the preset temperature. The compositions of the products were mainly CO and a corresponding amount of H_2S derived from COS, and the catalytic activity was calculated on the basis of the accumulated amount of H_2S. The compositions of the sulfur-containing gaseous products generated under different temperatures were analyzed using a gas chromatograph (GC-7890II) equipped with a flame photometric detector (FPD) and a Porapak Q column. Steady-state catalytic activity was measured at temperatures between 140 °C and 300 °C, in step of 20 °C. Based on the COS conversions of incoming [$c(COS)_{in}$] and effluent [$c(COS)_{out}$], COS conversion was calculated according to the equation

$$\text{Conv.}\% = \frac{c(COS)_{in} - c(COS)_{out}}{c(COS)_{in}} \times 100\% \qquad (1)$$

To obtain kinetic parameters, the reaction was carried out on a differential quartz reaction (with an inside diameter of 4 mm). In this case, in order to avoid the influent of the external and internal

mass transport resistance for ML-MoS$_2$/RGO catalyst, the gas flow was selected at 300 mL min^{-1}. 30 mg catalyst was used and the COS conversion was controlled in the less than 10% to minish systematic analysis error as well as the deviation resulted from reactant concentration change in the catalyst bed.

Specific reaction rate (r), rate constant (k) and apparent activation energy (E_a) were calculated according to the following equations:

$$r = \frac{F \times \text{Conv.\%}}{m_{\text{cat}}} \left(\text{mol} \cdot \text{s}^{-1} \cdot \text{g}_{\text{cat}}^{-1} \right) \tag{2}$$

In Eq. (2), F (mL min^{-1}) is the flow rate of COS; m_{cat} (g) is the amount of the catalyst. The apparent activation energy and kinetic parameters were determined based on the reaction data in the temperature ranges 513–543 K for ML-MoS$_2$/RGO, 513–553 K for FL-MoS$_2$/RGO, 573–633 K for B-MoS$_2$, according to Arrhenius equation. In the latter case, the COS concentrations were calculated at different temperature, the reaction order was confirmed to be the zero order by experiments with the excess of H$_2$. In the case of zero order, $k = r$.

3. Results and discussion

3.1. Synthesis and characterization of ML-MoS$_2$/RGO composites

Schematic illustration of the preparation of ML-MoS$_2$/RGO by a CTAB-assisted method was shown in Fig. 1a. It has been known that GO possesses a large number of oxygen-containing functional groups, such as −COOH and −OH, which facilitate the adsorption of cationic surfactant from solution onto the negatively charged GO surface because of the strong electrostatic interactions between them [48]. Therefore, we can obtain a suspension of CTA$^+$-adsorbed

GO by mixing GO and a CTAB solution together with stirring. It was obvious that GO is hydrophilic and insoluble in organic media such as chloroform shown in Fig. 1b. However, the color of the GO aqueous solution changes to clear after CTAB was added and chloroform solution color changes to dark brown, which implies that the hydrophilic surfaces of GO have been modified by the hydrophobic alkyl chains of CTAB and successfully transferred to the organic phase. The adsorption of CTA$^+$ on the GO surface renders the GO surface positively charged, which enhances the interaction between GO and anions such as MoS$_4^{2-}$ [46]. Under the hydrazine reduction at 95 °C, MoS$_4^{2-}$ adsorbed on the GO surface were reduced to MoS$_2$, simultaneous with the reduction of GO to RGO. Overall reaction as following [49]:

$$2MoS_4^{2-} + N_2H_4 = 2MoS_2 + N_2 + 2S^{2-} + 2H_2S \tag{3}$$
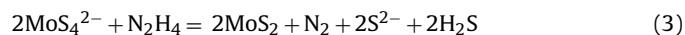
At the same time, the excess CTA$^+$ can insert between MoS$_2$ layers [50], leading to the increasing of MoS$_2$ interlayer space and the eventual formation of monolayer MoS$_2$. A composite mainly consisted of MoS$_2$ and RGO with adsorbed CTA$^+$ was obtained. With the subsequent heat treatment in N$_2$ at 800 °C for 2 h, the adsorbed CTA$^+$ was carbonized to amorphous carbon. The formed amorphous carbon can restrain the stacking of MoS$_2$ especially in (002) planes to promote the formation of monolayer MoS$_2$, similarly, the overlap of RGO can also be effectively prohibited to form monolayer RGO sheets. As a result, cross-overlap-covered structure consisted of monolayer MoS$_2$ nanosheets and RGO was prepared. However, FL-MoS$_2$/RGO was obtained in the absence of CTAB, in which few-layer MoS$_2$ was anchored on RGO uniformly. The stack of both MoS$_2$ nanosheets and RGO will take place to form their corresponding multilayer structures without the assistance of CTAB. In brief, the formation of monolayer MoS$_2$ was attributed to the synergistic effect between CTAB and GO.
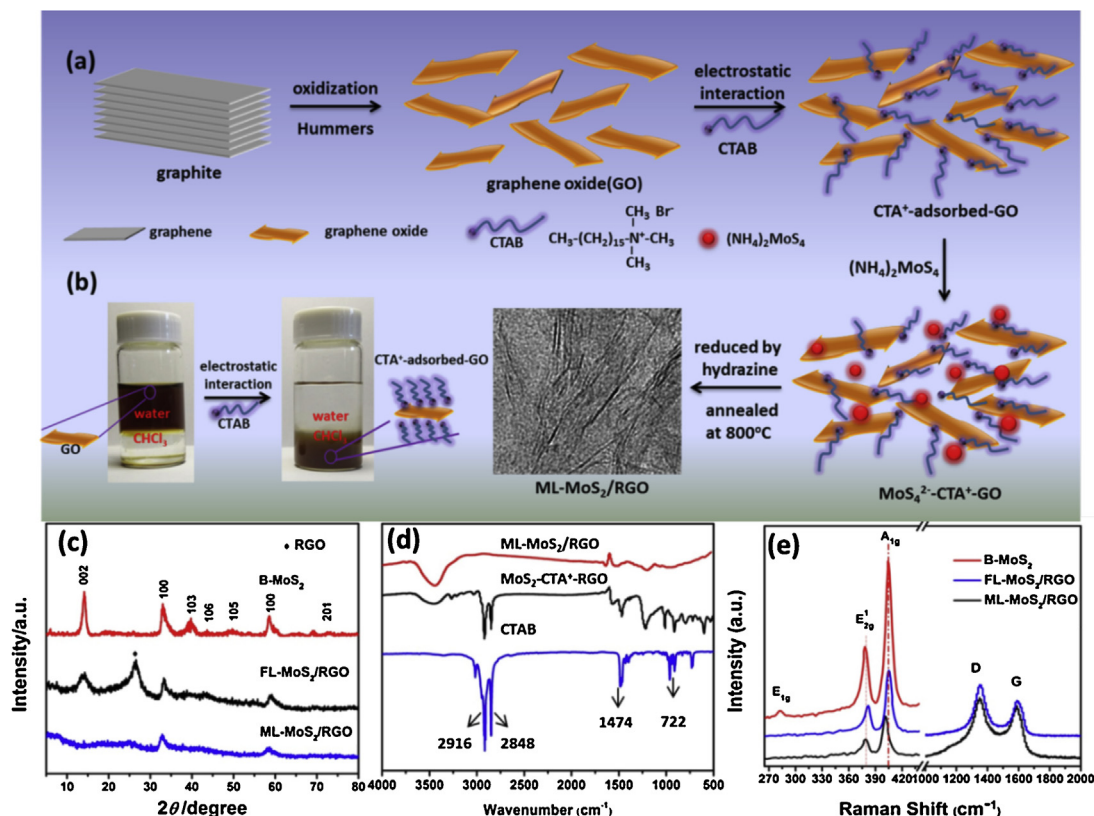
Fig. 1. (a) Schematic drawing of the preparation of ML-MoS$_2$/RGO by a CTAB-assisted method; (b) photographs of the GO solution during phase transfer process by CTAB; (c) XRD patterns of B-MoS$_2$, FL-MoS$_2$/RGO and ML-MoS$_2$/RGO samples; (d) FT-IR spectra of ML-MoS$_2$/RGO after heat-treating, ML-MoS$_2$/RGO before heat-treating (MoS$_2$–CTA$^+$-RGO) and CTAB; (e) Raman spectra of B-MoS$_2$, FL-MoS$_2$/RGO and ML-MoS$_2$/RGO samples.

The MoS_2/RGO nanocomposites were characterized by XRD as shown in Fig. 1c. X-ray diffraction (XRD) has been used as a simple and convenient method to judge MoS_2 whether as monolayer or multilayer based on the MoS_2 (002) peak. Fig. 1c shows the XRD patterns of B-MoS_2, FL-MoS_2/RGO and ML-MoS_2/RGO after annealing in N_2 atmosphere at 800 °C for 2 h. The diffraction peaks of annealed B-MoS_2 can be readily indexed to 2H-MoS_2 with a hexagonal structure (JCPDS-37-1492). The B-MoS_2 displays a strong peak (002) at $2\theta = 14.2°$, which indicates a well-stacked layered structure and the corresponding interlayer distance is about 0.62 nm. In the case of FL-MoS_2/RGO, we can observe most of the peaks attributed to MoS_2, however, these peaks are obviously weaker and broader compared to that of B-MoS_2. This indicates the low crystallinity and few layer feature of MoS_2, from which we can reasonably conclude that the presence of GO benefits the formation of few layer MoS_2 during the preparation process. It should be noticed that a strong peak ($2\theta = 26°$) attributed to overlapped RGO also exists in FL-MoS_2/RGO, similar to the RGO in Fig. S1. On the contrary, the XRD pattern of ML-MoS_2/RGO in Fig. 1b shows only two weak peaks at $2\theta = 32.9°$, and $58.6°$, which are ascribed to the (100) and (110) planes of 2H-MoS_2, respectively. The absence of (002) reflection evidences that there is no self-stacking of MoS_2 (002) plane in ML-MoS_2/RGO with only the monolayer MoS_2 in the composites. Furthermore, it can be seen that there is no obvious peak at $2\theta = 25.7°$ belonged to graphite, suggesting the presence of CTAB in ML-MoS_2/RGO sample also prohibit the restack of RGO nanosheets. XRD pattern of GO (Fig. S1) shows a major peak at $2\theta = 11°$ corresponding to an interlayer spacing of 0.8 nm, while RGO derived from hydrazine reduction of graphene oxide platelets give rise to a strong peak at $2\theta = 25.7°$, which indicates the serious restack of graphene during the reduction process [51].

The incorporation of CTA^+ into the samples has been confirmed by FT-IR analysis as shown in Fig. 1d. Prior to heat treatment, the CTA^+ adsorbed materials clearly display two peaks at 2916 and 2848 cm^{-1}, which belong to C—H stretching vibration of —CH_3 and —CH_2 in CTAB, respectively. The peak at 1474 cm^{-1} and 722 cm^{-1} are assigned to the asymmetric δ_{C-H} (rocking vibration) of —CH_3 and —CH_2, and the δ_{C-H} (bending vibration) of —CH_2 in long-chain alkanes, respectively. However, all of these peaks attributed to CTAB disappear completely after annealing at 800 °C because of the carbonization of CTAB. Our results indicates that CTA^+ may insert between MoS_2 layers and RGO layers, and transform into amorphous carbon interlaid between monolayer MoS_2 sheets after heat treatment.

The MoS_2/RGO nanocomposites were further characterized by Raman spectra as shown in Fig. 1e. Raman spectroscopy can be used to identify the number of MoS_2 layers by distinguishing the distance between A_{1g} and E^1_{2g} ($\Delta k = \nu (A_{1g}) - \nu (E^1_{2g})$) [52]. The Raman peaks at 378 cm^{-1} and 404 cm^{-1} are attributed to B-MoS_2 E^1_{2g} and A_{1g}, respectively, and the $\Delta k = 26 \, cm^{-1}$. While FL-MoS_2/RGO displays two Raman peaks at 382 cm^{-1} (E^1_{2g}) and 405 cm^{-1} (A_{1g}) ($\Delta k = 23 \, cm^{-1}$, as shown in Fig. 1e). As for the ML-MoS_2/RGO, there are two Raman peaks at 379 cm^{-1} (E^1_{2g}) and 401 cm^{-1} (A_{1g}) with $\Delta k = 22 \, cm^{-1}$. The Δk of FL-MoS_2/RGO (23 cm^{-1}) and ML-MoS_2/RGO (22 cm^{-1}) well agree with the few layer and monolayer MoS_2 sheets previously reported [50]. It has been pointed out that a blue shift of A_{1g} is observed with the decreasing of MoS_2 layer number when the layer number is less than 6 [52,53]. In addition, the suppression or absence of E_{1g} Raman peak in FL-MoS_2/RGO and ML-MoS_2/RGO may be attributed to the few-layer or monolayer structure of MoS_2 [54]. Fig. 1e also shows two dominant Raman peaks at 1350 cm^{-1} (D-band) and 1590 cm^{-1} (G-band) of graphene, which is well agreed with that of hydrazine-reduced GO [55]. The D-band is attributed to defects, edges and disorder in the hexagonal graphitic layers, while the G-band represents the vibration of sp^2 carbon atoms in a 2D hexagonal lattice. The relative intensity ratio of I_D/I_G can serve as a convenient measurement of defects in carbon materials [56,57]. The calculated values of I_D/I_G for ML-MoS_2/RGO and FL-MoS_2/RGO are 1.16 and 1.45, respectively. XRD and Raman characterization indicate that monolayer MoS_2 exists in ML-MoS_2/RGO composites, few-layer MoS_2 in FL-MoS_2/RGO composites and multilayer MoS_2 in B-MoS_2. The content
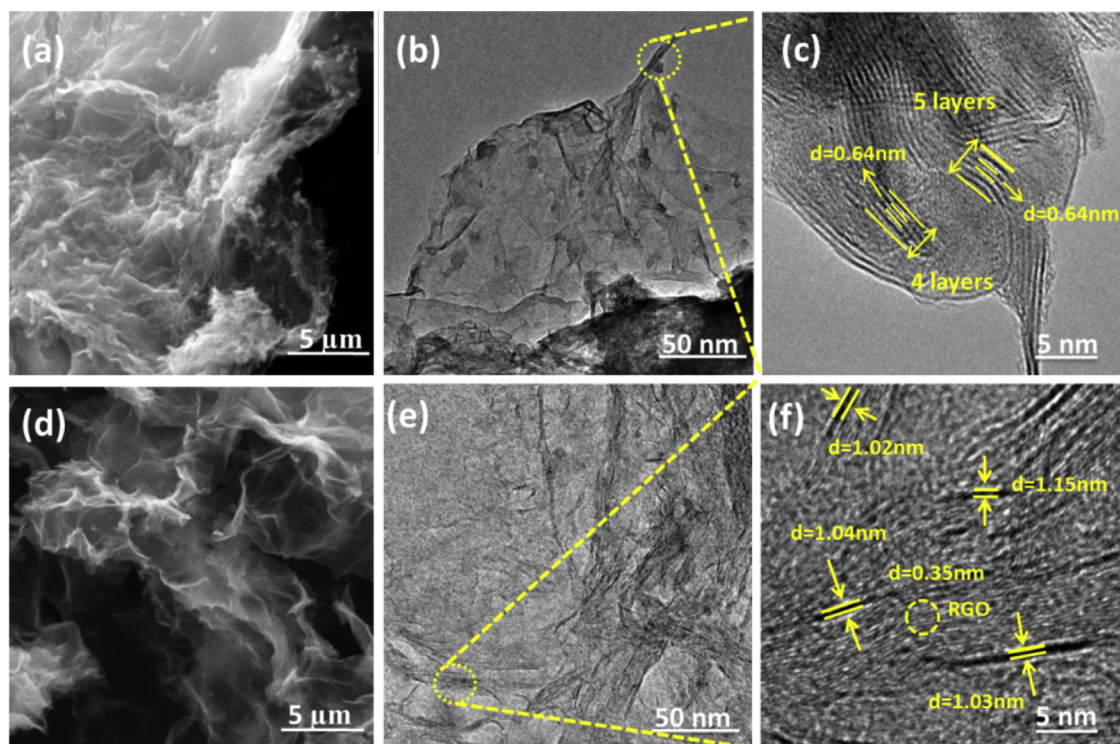

Fig. 2. (a) SEM image, (b) TEM image and (c) HRTEM image of FL-MoS_2/RGO; (d) SEM image, (e) TEM image and (f) HRTEM image of ML-MoS_2/RGO.
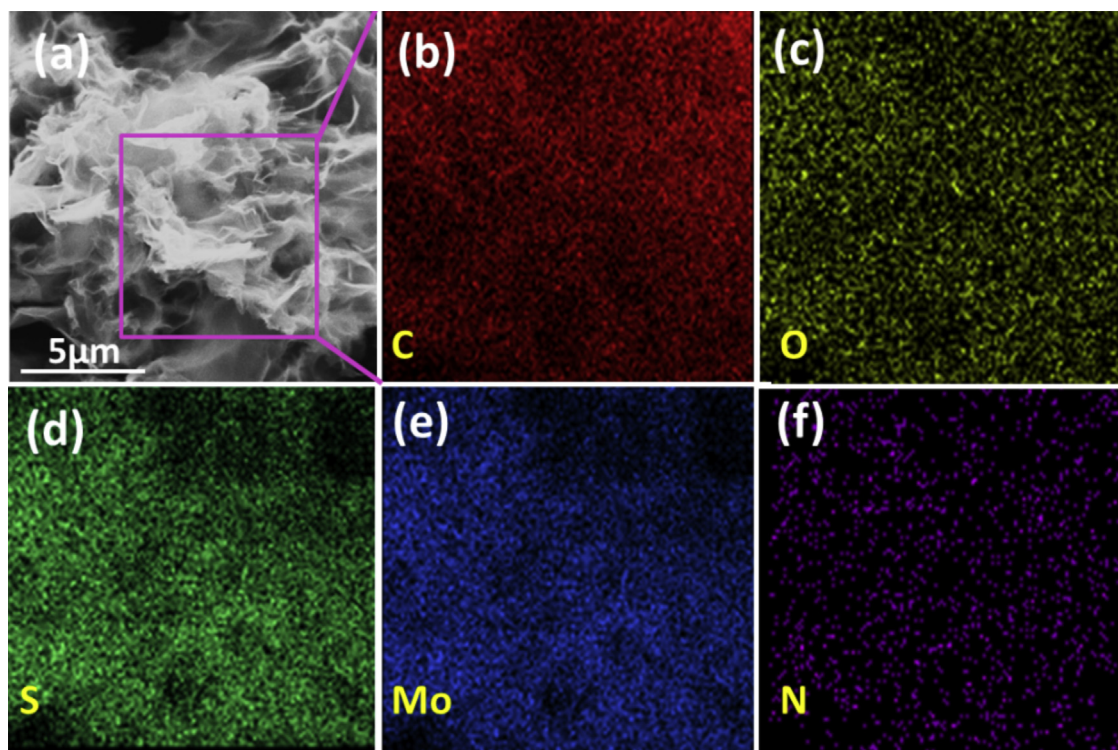
Fig. 3. (a) SEM image and (b–f) SEM-EDX element mapping of ML-MoS$_2$/RGO catalyst.

of MoS$_2$ calculated from TGA (shown in Fig. S2) in FL-MoS$_2$/RGO is 42.54%, which is approximately the same to the ML-MoS$_2$/RGO (43.41%).

In order to explore the layer structure of MoS$_2$ in the above mentioned catalysts, detailed investigation were further conducted by electron microscopies, including SEM, TEM and HRTEM (Fig. 2). The morphology of B-MoS$_2$ was also observed by SEM shown in Fig. S3, which displays large irregular particles with dense structure in micrometer scale. Fig. 2a exhibits the feature of FL-MoS$_2$/RGO composites obtained without CTAB, MoS$_2$ particles aggregate together on the surface of overlapping RGO. From the magnified image of FL-MoS$_2$/RGO sample in Fig. 2b, the agglomerated MoS$_2$ nanoparticles adhere to the surface of RGO. MoS$_2$ in FL-MoS$_2$/RGO composites has a well-layered structure with a $d_{(002)}$ = 0.64 nm measured from Fig. 2c, which well agreed with the 2H-MoS$_2$ crystal structure and

the XRD patterns. The number of MoS$_2$ layers is about 4–5, which suggests that the MoS$_2$ in FL-MoS$_2$/RGO composites is few-layer structure. The selective growth of MoS$_2$ on GO can be attributed to the interaction between the oxygen functional groups on GO sheets and Mo precursors [58]. GO nanosheets act as a novel substrate for MoS$_2$ nucleation and growth to form few layer MoS$_2$, and the serious stack and reunite of MoS$_2$ nanosheets could be inhibited by the presence of RGO. The microstructures of ML-MoS$_2$/RGO sample are shown in Fig. 2d. The uniform structures indicate that the MoS$_2$ layers are well supported on the curved RGO surface. As seen in the HRTEM (Fig. 2e), monolayer MoS$_2$ sheets are well supported on the curved RGO surface and highly dispersed in the composites. The interlayer distance between adjacent MoS$_2$ nanosheets measured in Fig. 2f is in range of 1.02–1.15 nm. We cannot observe the stacking of MoS$_2$ (002) planes, and this is consistent with the absence of
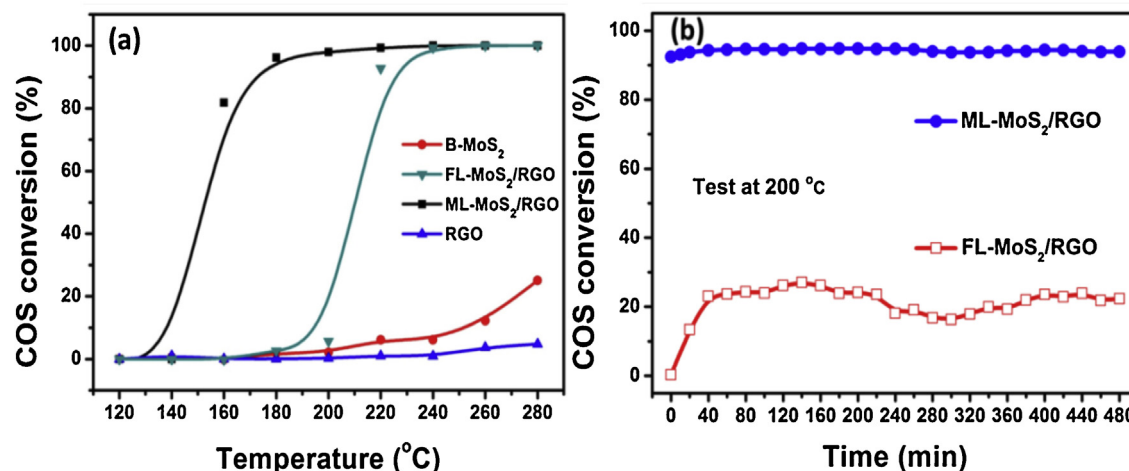

Fig. 4. (a) Temperature-dependent conversion of COS hydrogenation over B-MoS$_2$, FL-MoS$_2$/RGO, ML-MoS$_2$/RGO and RGO samples. (b) COS conversion as a function of time on stream over ML-MoS$_2$/RGO and FL-MoS$_2$/RGO catalysts at 200 °C. (Reaction conditions: 500 ppm COS, 10 vol% H$_2$, balanced with N$_2$, *GHSV* = 32000 h^{-1}).

the (002) reflection in XRD patterns (Fig. 1c). The amorphous carbon from the carbonization of CTAB can restrain the stacking of MoS_2 especially in (002) planes to facilitate the formation of monolayer MoS_2. Furthermore, amorphous carbon formed on the RGO also restrains the overlap of RGO. As a result, the as-formed monolayer MoS_2 nanosheets and RGO sheets give rise to the cross-overlap-covered structure. The most powerful evidence for this is that the sum of $d_{(002)}$ of MoS_2 (0.64 nm) and the interlayer of RGO (0.36 nm) is approximately equal to the interlayer distance between contiguous monolayer MoS_2 of about 1.0 nm.

The elemental distribution of ML-MoS_2/RGO composites was shown in Fig. 3, all of C, O, S, Mo, and N elements uniformly distribute on the whole nanosheet surface (N elements from CTAB). According to the EDX, the atomic ratio Mo/S of 1.08/2.20 is calculated which is close to the MoS_2 stoichiometry. Taking into all the results mentioned above, monolayer MoS_2 anchored on RGO composites has been successfully prepared by CTAB-assisted method.

3.2. HDS activity

In this study, B-MoS_2, FL-MoS_2/RGO, ML-MoS_2/RGO and RGO catalysts were investigated in the HDS of carbonyl sulfide. The catalytic properties have been compared in Fig. 4a. Obviously, the B-MoS_2 exhibits rather low HDS activity and the RGO show almost no catalytic activity in the test temperature range. It is clear that the ML-MoS_2/RGO exhibits remarkably higher catalytic activity than that of the FL-MoS_2/RGO within the temperature range employed. The start-up reaction takes place at about 135 °C in the case of ML-MoS_2/RGO, while for FL-MoS_2/RGO the temperature above 190 °C. The COS conversion reaches about 100% at 220 °C over ML-MoS_2/RGO, while the complete conversion over FL-MoS_2/RGO needs more than 240 °C. This reveals that an effective integration of monolayer MoS_2 nanosheets and RGO can lead to synergistic interaction between them for high catalytic activity. The high catalysis activity of ML-MoS_2/RGO can be ascribed to more exposure of MoS_2 active sites on monolayer MoS_2 and high dispersion of MoS_2 on RGO sheets. In fact, B-MoS_2 undoubtedly has a great quantity of active components, but it fails to materialize the completed removal of COS even at high temperature (300 °C), the poor dispersion and easy agglomeration of bulk MoS_2 particles at high temperature may be responsible for this phenomenon. Moreover, the low utilization of catalytic active components in bulk catalyst is a waste of resource. For comparison, traditional commercial activated carbon (AC) and activated aluminium oxide (γ-Al_2O_3) were also adopted as support materials, and the catalytic performances of MoS_2/AC and MoS_2/γ-Al_2O_3 prepared by the same method were evaluated. As shown in

Fig. S5, ML-MoS_2/RGO exhibits the most effective HDS activity in the three catalysts though they have the same loading amount of MoS_2, suggesting the advantage of RGO as support. Compared with γ-Al_2O_3, RGO-supported MoS_2 are more weakly bound to the support, which might be beneficial for a higher catalytic activity [27]. In the case of AC, the intricate micro-pore structure in AC would be unfavorable for the access of MoS_2 active sites to the reactant, whereas RGO has its advantage over AC due to the extended basal plane structure.

Furthermore, ML-MoS_2/RGO shows good catalysis stability. The plots of the COS conversion as a function of time on stream over ML-MoS_2/RGO was shown in Fig. 4c. As can be seen, the catalysts show almost no deactivation during 8 h on stream and the performance of the COS hydrodesulfurization over ML-MoS_2/RGO is significantly higher than that over FL-MoS_2/RGO at the same temperature. For example, FL-MoS_2/RGO keeps only 22.29% conversion of COS after 8 h on stream, however, ML-MoS_2/RGO keeps 93.8% conversion at the same time. The spent catalyst ML-MoS_2/RGO after 8 h on stream was characterized by HRTEM shown in Fig. S6. The image reveals a good stability on monolayer MoS_2 structure, which is the reason for the good catalysis stability.

3.3. H_2S selectivity

To deeply understand the different catalytic activity between FL-MoS_2/RGO and ML-MoS_2/RGO during the HDS process, we examines the H_2S yield as a function of COS conversion. Eq. (4) was utilized to evaluate the H_2S selectivity of the tested samples as follows:

$$X_{H_2S} = \frac{C_S}{C_{S_0}} \times 100\% \tag{4}$$

In this equation, X_{H_2S}, C_S and $C_{S,0}$ represents the H_2S selectivity, total H_2S in the product (ppm) streams and the theoretical value of H_2S (ppm) converted from the COS, respectively. Theoretically, COS can be transformed into H_2S completely, in other words, the selectivity to H_2S should be 100% from COS hydrogenation. However, the apparent selectivity of H_2S depends on the structure of catalysts and the reaction condition (Fig. 5). It can be seen from Fig. 5(a and b) the difference of the COS conversion and the corresponding H_2S selectivity between FL-MoS_2/RGO and ML-MoS_2/RGO were clear especially in the low temperature range, despite the rising tendency of the H_2S selectivity over two catalysts with the increasing temperature. It is noted that the H_2S selectivity is lower than 100% when the reaction temperature is below 340 °C for FL-MoS_2/RGO, while below 260 °C for ML-MoS_2/RGO,
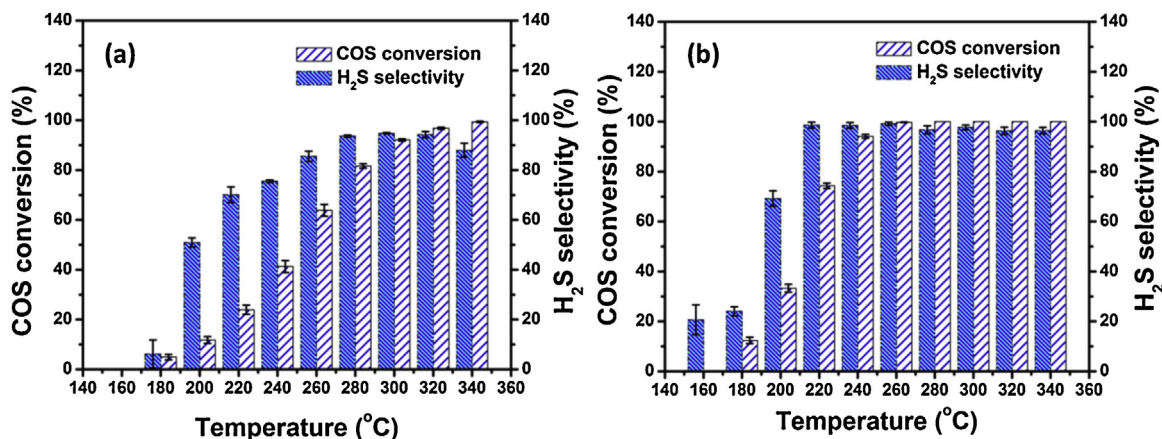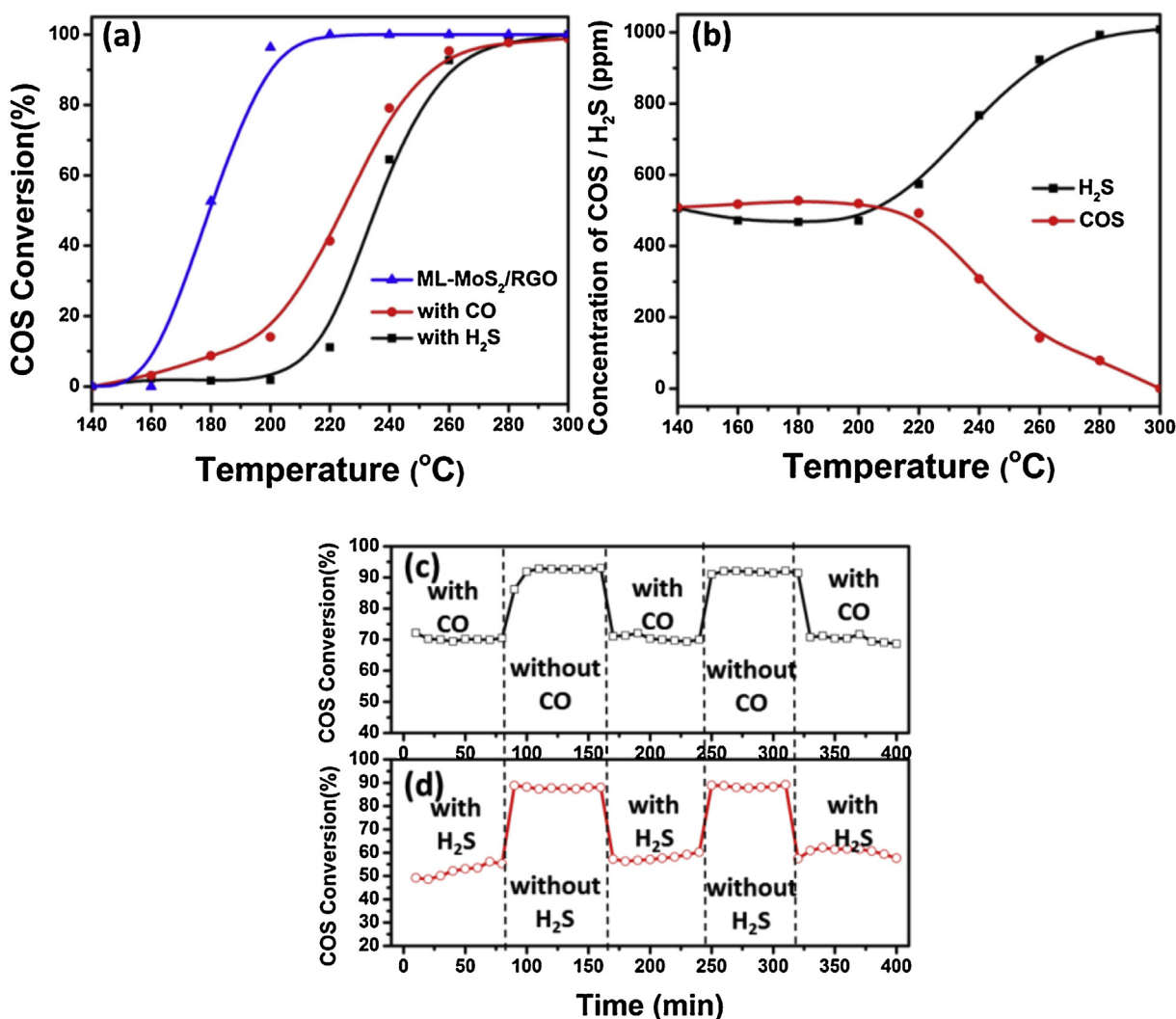

Fig. 5. Temperature-dependent conversion of COS hydrogenation and corresponding H_2S selectivity over (a) FL-MoS_2/RGO and (b) ML-MoS_2/RGO. (Reaction conditions: 1000 ppm COS, 10 vol% H_2, balanced with N_2, GHSV = 16000 h^{-1}).

Fig. 6. (a) Temperature-dependent conversion of COS hydrogenation over ML-MoS$_2$/RGO for feeding gas 500 ppm of COS/N$_2$ with 500 ppm H$_2$S or 800 ppm CO at GHSV = 32000 h^{-1}; (b) Temperature-dependent concentration of COS and H$_2$S over ML-MoS$_2$/RGO for feeding gas 500 ppm of COS/N$_2$ with 500 ppm H$_2$S at GHSV=32000 h^{-1}; (c) COS conversion over ML-MoS$_2$/RGO catalyst at 240 °C, feeding gas 500 ppm of COS/N$_2$ with or without 800 ppm CO at GHSV = 32000 h^{-1}; (d) COS conversion over ML-MoS$_2$/RGO catalyst at 240 °C, feeding gas 500 ppm of COS/N$_2$ with or without 500 ppm H$_2$S at GHSV = 32000 h^{-1}.

suggesting the adsorption of COS and formed H$_2$S on the surface of catalysts. At high temperatures, the catalytic reaction becomes dominant and the adsorption is ignorable to give rise to almost 100% H$_2$S selectivity over these MoS$_2$/RGO composite catalysts. It can be reasonably understood taking into consideration of the fact that carbon materials have been used as adsorbent for the removal of H$_2$S and COS [44]. In our case, the support materials for two catalysts are same as RGO, thus the distinction of the COS conversion and H$_2$S selectivity over both catalysts should be ascribed to the structure difference of active component, i.e. ML-MoS$_2$ and FL-MoS$_2$. Obviously, ML-MoS$_2$/RGO with monolayer structure performs better than FL-MoS$_2$/RGO in particular at low temperatures. H$_2$S selectivity is always below 100% in the temperature range employed, which means no excess H$_2$S is formed with the increasing of temperature, evidently demonstrates both FL-MoS$_2$/RGO and ML-MoS$_2$/RGO stable without the sulfur loss during hydrogenation process. The property-structure relationship between them is interesting and has been investigated by further characterization (see farther below).

3.4. Catalytic performance of the ML-MoS$_2$/RGO with impurities

Fig. 6a shows the COS conversion results over the ML-MoS$_2$/RGO catalyst for the feed gas of 500 ppm COS together with 500 ppm H$_2$S or 800 ppm CO in N$_2$. The inhibition effect of impurity gases on the reaction over the catalyst was remarkable at low temperature (<260 °C) while quite limited at high temperature (>260 °C). Over the catalyst, T_{100} (the temperature for COS conversion reaching 100%) of the reaction in the feeding gas of 500 ppm COS/N$_2$ was 220 °C. When H$_2$S (500 ppm) or CO (800 ppm) was introduced into the feed gas, respectively, T_{100} was increased to 300 °C. It can be observed from Fig. 6a that the effect of CO and H$_2$S on COS conversion decreases with the increasing of temperature. For example, the variation ranges of COS conversion in the presence of CO and H$_2$S at 200 °C was 57% and 94%, respectively. However, only 4% and 35% drop in COS conversion was shown with CO and H$_2$S at 240 °C, respectively.

Temperature-dependent concentration of COS and H$_2$S over ML-MoS$_2$/RGO with feeding gas of COS (500 ppm) and H$_2$S (500 ppm)

Table 1
Active sites of the catalysts and kinetic parameters of the reaction over the catalysts.

Cat.	T (°C)	$(k \times 10^{-6})$[a] (mol·s^{-1}·g^{-1})	Active sites[b] (µmol·g^{-1})	TOF[c] (s^{-1})	E_a[d] (kJ·mol^{-1})
ML-MoS$_2$/RGO	160	30.44	8.26		106.00
	180	35.80			
	200	36.46		4.41	
FL-MoS$_2$/RGO	180	0.97	7.63		113.84
	200	2.11		0.28	
	220	34.48			
B-MoS$_2$	200	0.80	3.82	0.21	114.15
	220	2.31			
	240	2.28			

[a] Evaluated from integral reaction of 500 ppm COS + N$_2$, *GHSV* = 32,000 h^{-1}.
[b] The data detected by CO pulse adsorption at room temperature.
[c] Calculated based on the data detected by integral reaction and CO pulse adsorption.
[d] Measured by differential reaction of 500 ppm COS + N$_2$, *GHSV* = 140,000 h^{-1}.

balanced with N$_2$ was shown in Fig. 6b. With the increasing of temperature, it can be indicated that the concentration of COS increased, while the concentration of H$_2$S decreased below 180 °C, which should be attributed to the adverse reaction of hydrogenation:

$$H_2S + CO = COS + H_2 \tag{5}$$

In this case, H$_2$S is extremely easy to transform into COS with the existence of CO. However, with the increasing temperature

from 200 to 300 °C, the concentration of COS decreased and the concentration of H$_2$S increased remarkably due to the favorable hydrogenation at high temperature.

$$COS + H_2 = H_2S + CO \tag{6}$$

In a word, it is easy for H$_2$S to transform into COS at low temperature while adverse reaction will take place at high temperature over ML-MoS$_2$/RGO.
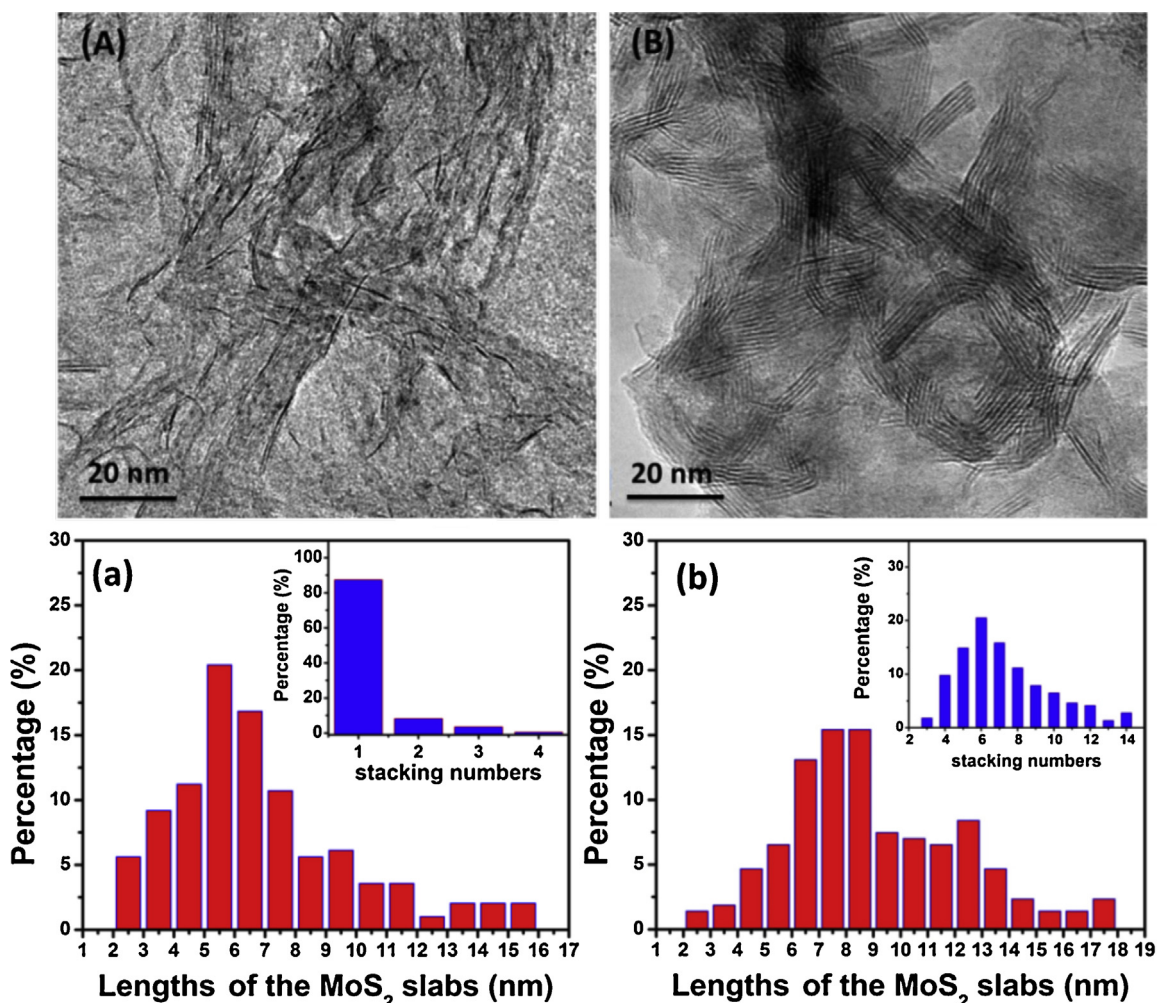
Fig. 7. HRTEM images of (A) ML-MoS$_2$/RGO and (B) FL-MoS$_2$/RGO; Statistics of the stacking numbers and lengths of the MoS$_2$ slabs of (a) ML-MoS$_2$/RGO and (b) FL-MoS$_2$/RGO.
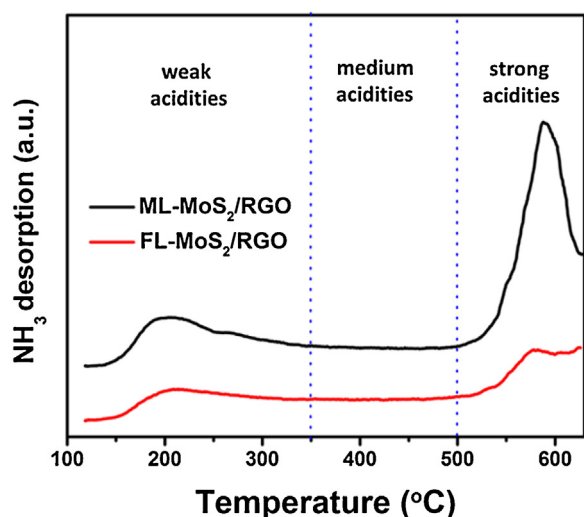
Fig. 8. The NH$_3$-TPD profiles of ML-MoS$_2$/RGO and FL-MoS$_2$/RGO.

Study on the effect of CO and H$_2$S on COS conversion with transient response method at 240 °C was shown in Fig. 6c and d. Due to the introductions of CO and H$_2$S, the COS conversion deceased to 70% and 57%, respectively, from the original 100% at 240 °C. The COS conversion could still reach surpass 90% when the impurity gases being cut off from the feeding gas. For the catalyst in the presence of impurity, although its initial activity was much lower than that in the absence of impurity, the activity did not further decline with time on stream. It means that the activity suppression due to the impurities is just caused by dynamics reason instead of catalyst poisoning and the ML-MoS$_2$/RGO catalyst displayed quite stable catalytic performance regardless of the presence or absence of CO and H$_2$S. With the existence of CO, the main reason for the decreasing conversion is the adverse reaction which makes H$_2$S extremely easy to transform into COS at low temperature. An excess of H$_2$S in the reactions would lead to adsorption on the active sites of ML-MoS$_2$/RGO to diminish active sites for COS hydrogenation.

3.5. Kinetic studies

In order to understand more detail in the HDS of COS over ML-MoS$_2$/RGO, we examined the kinetic parameters of this hydrogenation reaction. A zeroth reaction order in COS and a positive order, less than one, in H$_2$ was revealed (shown in Fig. S7). The data of kinetic parameters measured by integral reaction and apparent active energies (E_a) measured by differential reaction calculated from the slope of the Arrhenius plots (shown in Fig. S8) were summarized in Table 1. It can be clearly seen that the E_a value of ML-MoS$_2$/RGO (106 kJ mol^{-1}) is the lowest one among three catalysts, which is coincided with its superior catalytic performance shown in Fig. 4a. However, the E_a values were in the same level for these three catalysts, suggesting that the reaction mechanism was not changed with variation of layer structure of MoS$_2$. The most possible reason for the effective HDS activity of ML-MoS$_2$/RGO should be ascribed to the active site number increasing for monolayer MoS$_2$, which significantly influence the pre-exponential factor, k_0 in Arrhenius equation, $k = k_0 \exp(-E_a/RT)$.

The chemisorption of NO, O$_2$ or CO has been frequently and widely used to evaluate the dispersion of active phase in HDS catalyst [59,60]. In our work, the active sites on the catalyst surface were measured by CO pulse adsorption. They were 8.26 μmol g^{-1} for ML-MoS$_2$/RGO, 7.63 μmol g^{-1} for FL-MoS$_2$/RGO, and 3.82 μmol g^{-1} for B-MoS$_2$. On this basis, TOF of the reaction over the catalysts was calculated (Table 1), which indicates that the reaction occurs with 4.41 s^{-1} over ML-MoS$_2$/RGO at 200 °C, with 0.28 s^{-1} over FL-MoS$_2$/RGO, and with 0.21 s^{-1} over B-MoS$_2$. Clearly, the TOF of ML-MoS$_2$/RGO was 15.75 times larger than FL-MoS$_2$/RGO and 21 times larger than B-MoS$_2$. The larger TOF and the lower E_a of ML-MoS$_2$/RGO compared with those of FL-MoS$_2$/RGO and B-MoS$_2$ may be derived from the function of better dispersions and more exposed active sites of monolayer MoS$_2$.

3.6. The mechanism of ML-MoS$_2$/RGO improving the HDS reaction

The stacking numbers and lengths of the MoS$_2$ slabs were obtained from statistical analysis based on many HRTEM images. As

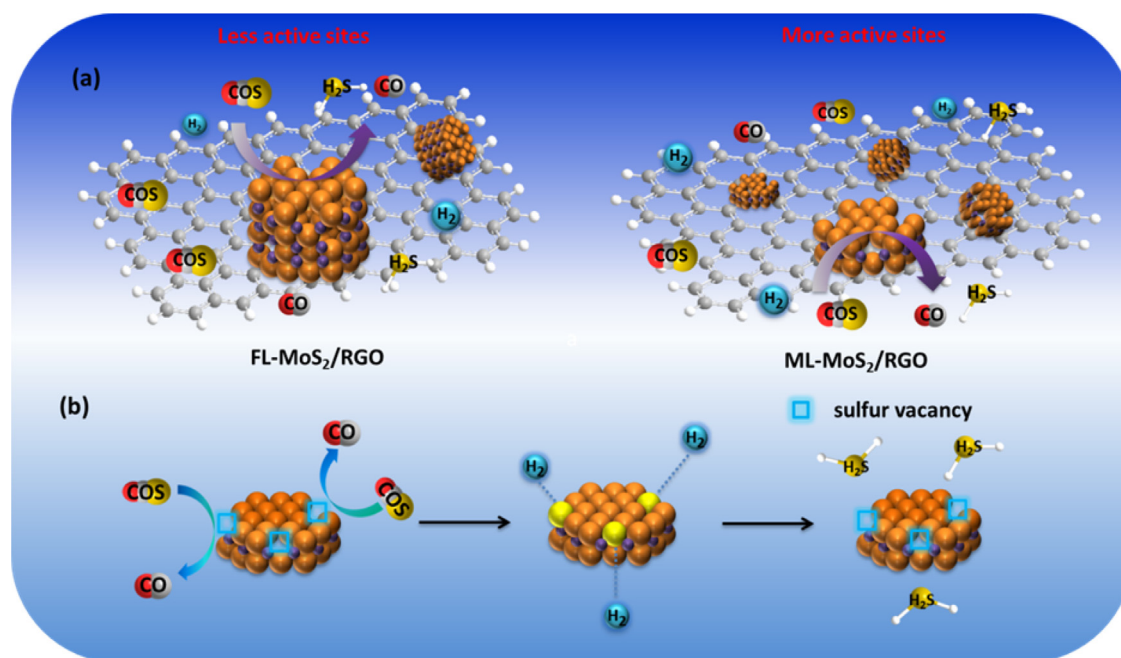**Fig. 9.** (a) Schematic illustration for the COS hydrogenation of FL-MoS$_2$/RGO and ML-MoS$_2$/RGO; (b) the COS hydrogenation model of ML-MoS$_2$/RGO catalyst.

shown in Fig. 7, it is obviously seen that the MoS_2 in ML-MoS_2/RGO is monolayer structure and the MoS_2 in FL-MoS_2/RGO is few-layer structure. The lengths and stacking distributions of ML-MoS_2/RGO and FL-MoS_2/RGO catalysts are shown in Fig. 7a and b respectively. The addition of CTAB leads to a decrease of average slab length from 8.4 nm to 6.4 nm and a decrease of average stacking number from 7 to 1. For ML-MoS_2/RGO, the percentage of monolayer MoS_2 could reach more than 85% which confirms that monolayer MoS_2 has been successfully prepared with the assistance of CTAB. The effective catalytic performance of removal COS can be attributed to the MoS_2 layer structure in the catalysts. MoS_2 with smaller stacking number and shorter length shows better catalytic activity due to its higher dispersion and more active sites for hydrogenation of COS.

The TPD of NH_3 is a useful tool to measure the acidity of the catalyst. The NH_3-TPD profiles for the ML-MoS_2/RGO and FL-MoS_2/RGO are completely different with each other as shown in Fig. 8. To compare the acidity distribution among the catalysts, the weak, medium, and strong acidities were assigned to the peak areas of NH_3-TPD curves below 350 °C, in 350–500 °C, and above 500 °C [61], respectively. Both ML-MoS_2/RGO and FL-MoS_2/RGO exhibit two peaks, one below 350 °C and another over 550 °C, which are attributed to the weak acid sites and strong acid sites, respectively. Several works proved that strong acid sites were closely related to hydrogenation activity [62,63], the higher acidity led to higher conversion. Combined with the zeroth-order reaction in COS verified in kinetic studies above, a strong adsorption of COS on the surface of catalyst ML-MoS_2/RGO can be achieved. The strong acid sites were regarded as catalysis active sites for COS to adsorb and lead to the hydriding reaction.

Based on the above observation, the catalytic mechanism is deduced and illustrated in Fig. 9. The apparent discrepancy between mono-layer and few-layer MoS_2 nanocrystals can be explained by the 2H stacking sequence of the MoS_2 nanocrystals that successively expose alternating Mo- and S-edge terminations [49]. As we know, the "Rim and Edge" model (shown in Fig. S9) has been widely accepted for the MoS_2 based catalyst during catalytic hydrogenation [7]. The rim sites are active in both hydrogenation and C—S bond rupture, while the edge sites active only in C—S rupture. It is evident that ML-MoS_2/RGO catalyst with monolayer structure shows more rim sites than FL-MoS_2/RGO composites under the same loading amount of MoS_2 (Fig. 9a). Coincided with statistics of the stacking numbers and lengths of the MoS_2 slabs, ML-MoS_2/RGO has the smaller stacking number and the shorter length of MoS_2 than FL-MoS_2/RGO, which proved a better dispersion of MoS_2 in ML-MoS_2/RGO. Sulfur vacancy at rim sites might function lower degree of steric hindrance for the adsorption and easily acts as the active sites for the extraction of S from a balancing source of S (e.g., COS, $COS + MoS_{2-x} \rightarrow MoS_2 + CO$), which conforms with the selectivity to H_2S much lower than 100% at low temperature (shown in Fig. 5) because of COS adsorption. Subsequently, H_2 reacts with MoS_2 to extract S from the edge of MoS_2 ($MoS_2 + H_2 \rightarrow MoS_{2-x} + H_2S$) to compete the catalytic hydrogenation process [64]. As shown in NH_3-TPD, the ML-MoS_2/RGO obviously has much more strong acid sites than FL-MoS_2/RGO. Since the COS on the surface of catalyst ML-MoS_2/RGO is a more strong adsorption, COS will be easily adsorbed on its surface compared with FL-MoS_2/RGO, which may be the reason for the ML-MoS_2/RGO holds the most effective HDS activity to remove COS.

The schematic illustration for the catalytic hydrogenation of COS over ML-MoS_2/RGO was shown in Fig. 9b. Monolayer MoS_2 nanosheets anchored on RGO exposes more defect sites or rim sites than few-layer MoS_2, resulting in its high catalytic activity in the COS hydrogenation. Hydrogen will react and remove the sulfur at

the edge of monolayer MoS_2, the formed sulfur vacancy adsorbs COS and extracts sulfur, then CO were released at the same time.

4. Conclusion

In summary, monolayer MoS_2 supported on RGO composites has been prepared through a facile liquid phase synthesis method. Hydrodesulfurization of COS over the catalysts was used as a model reaction to utilize the well-established structure-reactivity relationship in elucidating the structure of the graphene-MoS_2 composites. The synergistic action of monolayer MoS_2 nanosheets and RGO sheets has been maximized by an effective integration, which is demonstrated by the interesting fact that the order of catalytic activity is as follows: monolayer MoS_2/RGO > few-layer MoS_2/RGO > unsupported bulk MoS_2. ML-MoS_2/RGO composites exhibit uniform and separated 2D monolayer MoS_2 nanosheets and thus possess a large number of active sites, making its best catalytic performance for the removal of COS at low temperature. Therefore, the monolayer MoS_2 combined with the unique structure of graphene would become a promising strategy for preparation of HDS catalysts with excellent catalytic activity.

Appendix A. Supplementary data

Supplementary data associated with this article can be found, in the online version, at http://dx.doi.org/10.1016/j.apcatb.2016.07.006.

References

[1] H.H. Yi, S.Z. Zhao, X.L. Tang, P. Ning, H.Y. Wang, D. He, Catal. Commun. 12 (2011) 1492–1495.
[2] X.Z. Wang, L. Ding, Z.B. Zhao, W.Y. Xu, B. Meng, J.S. Qiu, Catal. Today 175 (2011) 509–514.
[3] J.J. Lee, H. Kim, J.H. Koh, A. Jo, S.H. Moon, Appl. Catal. B: Environ. 58 (2005) 89–95.
[4] S. Il Lee, A. Cho, J.H. Koh, S.H. Oh, S.H. Moon, Appl. Catal. B: Environ. 101 (2011) 220–225.
[5] D.W. Gao, A.J. Duan, X. Zhang, Z. Zhao, E. Hong, J.M. Li, H. Wang, Appl. Catal. B: Environ. 165 (2015) 269–284.
[6] L. Pena, D. Valencia, T. Klimova, Appl. Catal. B: Environ. 147 (2014) 879–887.
[7] M. Daage, R.R. Chianelli, J. Catal. 149 (1994) 414–427.
[8] H. Farag, K. Sakanishi, M. Kouzu, A. Matsumura, Y. Sugimoto, I. Saito, Ind. Eng. Chem. Res. 42 (2003) 306–310.
[9] E. Devers, P. Afanasiev, B. Jouguet, M. Vrinat, Catal. Lett. 82 (2002) 13–17.
[10] B. Yoosuk, J.H. Kim, C. Song, C. Ngamcharussrivichai, P. Prasassarakich, Catal. Today 130 (2008) 14–23.
[11] K.A. Carrado, J.H. Kim, C.S. Song, N. Castagnola, C.L. Marshall, M.M. Schwartz, Catal. Today 116 (2006) 478–484.
[12] I. Bezverkhyy, P. Afanasiev, M. Lacroix, J. Catal. 230 (2005) 133–139.
[13] H. Farag, A.N.A. El-Hendawy, K. Sakanishi, M. Kishida, I. Mochida, Appl. Catal. B: Environ. 91 (2009) 189–197.
[14] H.P. Zhang, H.F. Lin, Y. Zheng, Y.F. Hu, A. MacLennan, Appl. Catal. B: Environ. 165 (2015) 537–546.
[15] D. Valencia, T. Klimova, Appl. Catal. B: Environ. 129 (2013) 137–145.
[16] C.T. Tye, K.J. Smith, Catal. Today 116 (2006) 461–468.
[17] A. Cho, S.H. Moon, Catal. Surv. Asia 14 (2010) 64–74.
[18] J.J. Lee, H. Kim, S.H. Moon, Appl. Catal. B: Environ. 41 (2003) 171–180.
[19] E.J.M. Hensen, P.J. Kooyman, Y. van der Meer, A.M. van der Kraan, V.H.J. de Beer, J.A.R. van Veen, R.A. van Santen, J. Catal. 199 (2001) 224–235.
[20] H. Schweiger, P. Raybaud, G. Kresse, H. Toulhoat, J. Catal. 207 (2002) 76–87.
[21] S. Eijsbouts, J.J.L. Heinerman, H.J.W. Elzerman, Appl. Catal. A: Gen. 105 (1993) 53–68.
[22] N. Zhang, S.Y. Gan, T.S. Wu, W.G. Ma, D.X. Han, L. Niu, ACS Appl. Mater. Interfaces 7 (2015) 12193–12202.
[23] P.P. Wang, H.Y. Sun, Y.J. Ji, W.H. Li, X. Wang, Adv. Mater. 26 (2014) 964–969.
[24] A.I. Dugulan, J.A.R. van Veen, E.J.M. Hensen, Appl. Catal. B: Environ. 142 (2013) 178–186.

[25] H. Farag, Appl. Catal. B: Environ. 84 (2008) 1–8.
[26] H. Farag, I. Mochida, K. Sakanishi, Appl. Catal. A: Gen. 194 (2000) 147–157.
[27] M. Breysse, P. Afanasiev, C. Geantet, M. Vrinat, Catal. Today 86 (2003) 5–16.
[28] K.S. Novoselov, A.K. Geim, S.V. Morozov, D. Jiang, Y. Zhang, S.V. Dubonos, I.V. Grigorieva, A.A. Firsov, Science 306 (2004) 666–669.
[29] A.K. Geim, K.S. Novoselov, Nat. Mater. 6 (2007) 183–191.
[30] M.D. Stoller, S.J. Park, Y.W. Zhu, J.H. An, R.S. Ruoff, Nano Lett. 8 (2008) 3498–3502.
[31] X.N. Guo, Z.F. Jiao, G.Q. Jin, X.Y. Guo, ACS Catal. 5 (2015) 3836–3840.
[32] J.F. Ping, Y.B. Zhou, Y.Y. Wu, V. Papper, S. Boujday, R.S. Marks, T.W.J. Steele, Biosens. Bioelectron. 64 (2015) 373–385.
[33] J. Yang, C.G. Tian, L. Wang, H.G. Fu, J. Mater. Chem. 21 (2011) 3384–3390.
[34] L. Liao, J. Zhu, X.J. Bian, L.N. Zhu, M.D. Scanlon, H.H. Girault, B.H. Liu, Adv. Funct. Mater. 23 (2013) 5326–5333.
[35] A.J. Smith, Y.H. Chang, K. Raidongia, T.Y. Chen, L.J. Li, J. Huang, Adv. Energy Mater. 4 (2014).
[36] D.H. Youn, S. Han, J.Y. Kim, J.Y. Kim, H. Park, S.H. Choi, J.S. Lee, ACS Nano 8 (2014) 5164–5173.
[37] K. Chang, W.X. Chen, Chem. Commun. 47 (2011) 4252–4254.
[38] K. Chang, W.X. Chen, ACS Nano 5 (2011) 4720–4728.
[39] J. Peng, J. Weng, Carbon 94 (2015) 568–576.
[40] Q.J. Xiang, J.G. Yu, M. Jaroniec, J. Am. Chem. Soc. 134 (2012) 6575–6578.
[41] L.L. Yu, Y.H. Lee, X. Ling, E.J.G. Santos, Y.C. Shin, Y.X. Lin, M. Dubey, E. Kaxiras, J. Kong, H. Wang, T. Palacios, Nano Lett. 14 (2014) 3055–3063.
[42] K. Roy, M. Padmanabhan, S. Goswami, T.P. Sai, G. Ramalingam, S. Raghavan, A. Ghosh, Nat. Nanotechnol. 8 (2013) 826–830.
[43] J. Peng, J. Weng, Biosens. Bioelectron. (2015), http://dx.doi.org/10.1016/j.bios.2015.12.034.
[44] K. Sakanishi, Z.H. Wu, A. Matsumura, I. Saito, T. Hanaoka, T. Minowa, M. Tada, T. Iwasaki, Catal. Today 104 (2005) 94–100.
[45] B.F. Machado, P. Serp, Catal. Sci. Technol. 2 (2012) 54–75.
[46] Z. Wang, T. Chen, W.X. Chen, K. Chang, L. Ma, G.C. Huang, D.Y. Chen, J.Y. Lee, J. Mater. Chem. A 1 (2013) 2202–2210.
[47] G. Berhault, A. Mehta, A.C. Pavel, J.Z. Yang, L. Rendon, M.J. Yacaman, L.C. Araiza, A.D. Moller, R.R. Chianelli, J. Catal. 198 (2001) 9–19.
[48] K. Zhang, L. Mao, L.L. Zhang, H.S.O. Chan, X.S. Zhao, J.S. Wu, J. Mater. Chem. 21 (2011) 7302–7307.
[49] P. Afanasiev, G.F. Xia, G. Berhault, B. Jouguet, M. Lacroix, Chem. Mater. 11 (1999) 3216–3219.
[50] G.C. Huang, T. Chen, W.X. Chen, Z. Wang, K. Chang, L. Ma, F.H. Huang, D.Y. Chen, J.Y. Lee, Small 9 (2013) 3693–3703.
[51] S. Park, J. An, J.R. Potts, A. Velamakanni, S. Murali, R.S. Ruoff, Carbon 49 (2011) 3019–3023.
[52] C. Lee, H. Yan, L.E. Brus, T.F. Heinz, J. Hone, S. Ryu, ACS Nano 4 (2010) 2695–2700.
[53] K.M. McCreary, A.T. Hanbicki, J.T. Robinson, E. Cobas, J.C. Culbertson, A.L. Friedman, G.G. Jernigan, B.T. Jonker, Adv. Funct. Mater. 24 (2014) 6449–6454.
[54] V.O. Koroteev, L.G. Bulusheva, I.P. Asanov, E.V. Shlyakhova, D.V. Vyalikh, A.V. Okotrub, J. Phys. Chem. C 115 (2011) 21199–21204.
[55] C. Bosch-Navarro, E. Coronado, C. Marti-Gastaldo, J.F. Sanchez-Royo, M.G. Gomez, Nanoscale 4 (2012) 3977–3982.
[56] S. Osswald, M. Havel, Y. Gogotsi, J. Raman Spectrosc. 38 (2007) 728–736.
[57] Z.H. Ni, Y.Y. Wang, T. Yu, Z.X. Shen, Nano Res. 1 (2008) 273–291.
[58] Y.G. Li, H.L. Wang, L.M. Xie, Y.Y. Liang, G.S. Hong, H.J. Dai, J. Am. Chem. Soc. 133 (2011) 7296–7299.
[59] R. Burch, A. Collins, Appl. Catal. 17 (1985) 273–308.
[60] T. Kubota, K. Sato, A. Kato, Usman, T. Ebihara, T. Fujikawa, Y. Araki, K. Ishida, Y. Okamoto, Appl. Catal. A: Gen. 290 (2005) 17–24.
[61] L.H. Ding, Y. Zheng, Z.S. Zhang, Z. Ring, J.W. Chen, J. Catal. 241 (2006) 435–445.
[62] J.A.R. Vanveen, H.A. Colijn, P.A.J.M. Hendriks, A.J. Vanwelsenes, Fuel Process. Technol. 35 (1993) 137–157.
[63] D. Ferdous, A.K. Dalai, J. Adjaye, Appl. Catal. A: Gen. 260 (2004) 153–162.
[64] G.C.A. Schuit, B.C. Gates, AIChE J. 19 (1973) 417–438.